

Imperial College London

Department of Mechanical Engineering
South Kensington, London, SW7 2AZ

ME4 Computational Fluid Dynamics

*Analysis of the Flow around an Aircraft
Project Assignment II*

Authors – Poppy Fryer, Henry Hart, Gordon Kumar, Leo Pashov, Sophie Smith

CIDs – 01191270, 01190775, 01195056, 01187364, 01191522

Course Leader – Prof. Pavlos Aleiferis

Date – 12th March 2020

Page Count – 28

Page Limit – 28

Abstract

A study was conducted into the flow physics of a Hercules C130 aircraft through the means of the CFD software STAR-CCM+. A mesh refinement study and analysis of three turbulence models were carried out using a model of half the plane. The turbulence models considered were: standard $k - \epsilon$ two-layer all y_w^+ treatment, SST $k - \omega$ and quadratic pressure strain Reynolds stress with high y_w^+ treatment. The drag and lift coefficients for different angles of attack were computed and compared for each turbulence model alongside qualitative analysis. The take off speed was also calculated using each model.

The mesh size was limited to roughly 2 million cells. This was compared to meshes of approximately 4 million and 200,000 to ensure the results were not distorted by the mesh. A prism layer mesher was used alongside the surface remesher, trimmer and volumetric controls to create a suitable grid and ensure reasonable y^+ values. From qualitative analysis, separation was found at 10° angle of attack using the $k - \omega$ model only. This effect was also reflected in lower lift and higher drag at this angle of attack. The lift and drag coefficient trends were found to agree with existing literature. Take-off speeds for the three models were all found to be roughly 62 ms^{-1} .

This study should be considered preliminary work due to the constraints of the mesh. In future, grid independence should be investigated further and using finer intervals of angle of attack would allow for more study into the onset of separation with the $k - \omega$ model. The take off speed could also be compared for a range of scenarios and ground effects could be included. However, overall the results of this study broadly agree with the expected results based on existing literature.

Contents

1	Introduction	2
1.1	Physical Problem Overview	2
1.2	Dimensionless Numbers	2
1.3	Objectives	3
2	Methodology	5
2.1	CAD Model	5
2.2	Boundary Conditions	5
2.3	Flow Physics	5
2.4	Wall Treatment	6
2.5	Mesh	7
2.6	Turbulence Models	9
3	Results and Discussion	12
3.1	Grid Refinement Study	12
3.2	Analysis of Flight Physics	14
4	Future Work	22
5	Conclusions	24
6	References	25

Nomenclature

a	Speed of sound;
C_D	Drag coefficient;
C_L	Lift coefficient;
D	Drag;
k	Turbulent kinetic energy;
γ	Ratio of specific heats;
μ	Dynamic viscosity;
ν	Kinematic viscosity;
$\bar{\phi}$	Time averaged quantity;
ϕ'	Reynolds decomposed fluctuating quantity;
ρ	Density;
τ_w	Wall shear stress;
A	Wing area;
L	Lift force;
l	Length scale;
P	Static pressure;
R	Gas constant for air;
Re	Reynolds number;
T	Static temperature;
u	Velocity;
u_τ	Friction velocity;
y	Distance to wall;

1. Introduction

1.1 Physical Problem Overview

The second coursework assignment for the MECH97012 ME4 Computational Fluid Dynamics course uses the STAR-CCM+ software to analyse the aerodynamic properties of a Hercules C130 aircraft. A scaled down half-model of the aircraft was provided. The model was scaled to the correct size and placed into a simulated wind-tunnel of appropriate dimensions. It should be noted that a wind-tunnel of this size is not practical in real life. The model used was a simplified representation of the aircraft without propellers, tail plane or engine effects.

1.2 Dimensionless Numbers

This simulation of aircraft flow is dependant on a collection of dimensionless numbers. In order for any simulation to be realistic, the key dimensionless numbers must be matched.

1.2.1 Reynolds Number

The Reynolds number is a measure of the ratio of inertial to viscous effects in a flow, and can be used to classify the flow in terms of where it will become turbulent. The Reynolds number is defined as follows:

$$Re = \frac{\rho ul}{\mu} \quad (1.1)$$

The speed is taken to be 150 ms^{-1} , density to be 0.5 kgm^{-3} as per the standard atmosphere at cruise height, dynamic viscosity to be $1.6 \times 10^{-5} \text{ kgm}^{-1}\text{s}^{-1}$ and the length to be the chord length of 5 m [1]. This gives a Reynolds number as below:

$$Re = \frac{0.5 \times 150 \times 5}{1.6 \times 10^{-5}} = 23.4 \times 10^6 \quad (1.2)$$

This implies that the flow will become turbulent at some point along the wing surface, and so selection of a turbulence model is critical for flight physics.

1.2.2 Mach Number

The Mach number gives the ratio of reference speed to the speed of sound. The global Mach number for this flow uses the flight speed as the reference and is given as below:

$$Ma = \frac{u}{a} = \frac{u}{\sqrt{\gamma RT}} = \frac{150}{309} = 0.49 \quad (1.3)$$

Given that the global Mach number is greater than 0.3, it will be treated as compressible. The Mach number is low enough however that shock waves are not expected to form on the wing surfaces, despite the local acceleration induced by the low pressure surface on top of the wing.

1.2.3 Lift and Drag Coefficients

The lift and drag coefficients are measures of aerodynamic performance that are critical to the efficiency and capability of the aircraft. These coefficients will be used and discussed throughout this report and are defined as follows:

$$C_L = \frac{L}{\frac{1}{2}\rho u^2 A} \quad (1.4)$$

$$C_D = \frac{D}{\frac{1}{2}\rho u^2 A} \quad (1.5)$$

1.3 Objectives

This report aims to detail the results of the following studies:

1. **Grid refinement study.** The default resolution for the included analyses involves the use of 2 million cells. The refinement study aims to show that the simulation is grid independent at this resolution. This is detailed in Section 3.1.
2. **Qualitative turbulence model comparison.** This report considers three turbulence models. These are as follows:
 - a. Standard $k - \epsilon$ two-layer all y_w^+ treatment.

- b. SST $k - \omega$.
- c. Quadratic pressure strain Reynolds stress with high y_w^+ treatment.

The turbulence models listed here are discussed further in Section 2.6. The qualitative reproduction of the flow will be compared across these turbulence models and different angles of attack using the coloured field visualisation tools in STAR-CCM+. This is detailed in Section 3.2.1.

3. **Take-off speed turbulence model comparison.** The turbulence model used will affect all aspects of the simulation, including the maximum achievable C_L and by extension the take-off speed. This is detailed in Section 3.2.3.
4. **Lift turbulence model comparison.** The coefficient of lift is also affected by turbulence model. The coefficient of lift will be compared across turbulence models and angles of attack in Section 3.2.2.
5. **Drag turbulence model comparison.** The coefficient of drag is also affected by turbulence model. The coefficient of drag will be compared across turbulence models and angles of attack in Section 3.2.2.

2. Methodology

2.1 CAD Model

The control volume used for this analysis consisted of a half-model of the aeroplane whose plane of symmetry was aligned with one of the six wind-tunnel walls. The five other walls were arranged such that the following best-practice clearances were observed:

1. 2 lengths' clearance to the bow.
2. 5 lengths' clearance to the stern.
3. 1.5 spans' clearance to port (and therefore starboard in real life).
4. 2.5 heights' clearance above and below.

2.2 Boundary Conditions

The boundary conditions used in all simulations were as follows:

1. **Wind tunnel top and bottom walls:** Slip wall.
2. **Wind tunnel port wall (beyond the wing tip):** Slip wall.
3. **Wind tunnel wall aligned with aeroplane symmetry plane:** Symmetry plane.
4. **Aeroplane surface:** No slip wall.
5. **Bow wall:** Velocity inlet.
6. **Stern wall:** Pressure outlet.

2.3 Flow Physics

All simulations used the following flow physics settings in order to accurately represent the real world flow:

1. **Steady:** While trailing vortices may be unsteady, the forces and speeds of interest in this study are not expected to be significantly oscillatory.

2. **Three dimensional flow:** Aeroplanes are not sufficiently simple in geometry to be simplified into a two dimensional shape. In some cases, a wing cross section may be appropriate to analyse using two dimensional simplifications.
3. **Ideal gas.** Due to the high Mach number (see Section 1.2.2), the flow is considered compressible and so constant density cannot be assumed. The temperature, pressure and density changes will be modelled using the ideal gas equation, which is appropriate for air.
4. **Segregated flow and energy:** The equations for velocity and enthalpy will be solved in a segregated fashion due to the limited computing resources available.

2.3.1 Solver Details

All relaxation factors were left at the STAR-CCM+ default values. Reference values for the physics conditions are given in Table 2.1 for cruise and take-off conditions. Second-order upwind convection schemes were used for all segregated properties. Every flow case was initially solved using the $k - \epsilon$ turbulence model before running the other turbulence models. If these simulations failed to converge, laminar solutions were found and used to initialise the $k - \epsilon$ simulations. If simulations failed to converge (regardless of turbulence model), constant density solutions were computed to initialise the compressible simulations. Simulations were considered converged if residuals were steady for over 500 iterations.

Table 2.1: Reference values for different operating conditions;

Quantity	Cruise	Take-off
$\rho(kg/m^3)$	0.5	1.041
$P_{abs}(kPa)$	33.0	101.325
Inlet Axial Velocity ($m s^{-1}$)	150.0	-

2.4 Wall Treatment

y^+ is an important dimensionless measure of grid point location, and is particularly useful to examine near the shear walls of a simulation. It is defined as follows:

$$y^+ = \frac{yu_\tau}{\nu} \quad (2.1)$$

Where y is the distance to the wall, ν is the kinematic viscosity of the fluid and u_τ is the friction velocity defined as follows, where τ_w is the wall shear stress:

$$u_\tau = \sqrt{\tau_w / \rho} \quad (2.2)$$

y^+ ranges from zero at the wall and increases to infinity at an infinite distance away from the wall. In real space, this range is continuous. In computational space, however, this range of y^+ is discretised. The value of y^+ at the first node centre away from the wall is known as y_w^+ . The value of y_w^+ over the surface of the shear wall is an important measure of grid quality at each point. A smaller value of y_w^+ is universally desirable from an accuracy perspective, however it is computationally demanding. Areas where the flow characteristics are critical to the overall results should be prioritised for low y_w^+ .

In the case of 'low' grid quality, where $30 < y_w^+ < 200$ [2] and therefore the first cell is in the log-law region of the near-wall flow, a wall-function approach is generally taken where the velocity profile is set as one that has been semi-analytically derived (i.e. Inner Law [3]). In Star CCM+, this approach is known as High y_w^+ treatment.

In the case of 'high' grid quality, the simulation is run all the way to the wall. This is known as wall-resolved. In this case, the y_w^+ should be < 5 and 20-30 cells should be used to simulate the inner wall region [2]. In Star CCM+ this is known as Low y_w^+ treatment. A two-layer approach uses a wall-function very near the wall and switches to wall-resolved further away.

All y_w^+ treatment selects either High or Low y_w^+ treatment depending on the grid quality encountered in the mesh. From the ranges of y_w^+ prescribed above, it is notable that there is a 'blind spot' for $5 < y_w^+ < 30$ and in this region (the buffer layer), All y_w^+ treatment performs at its worst [2].

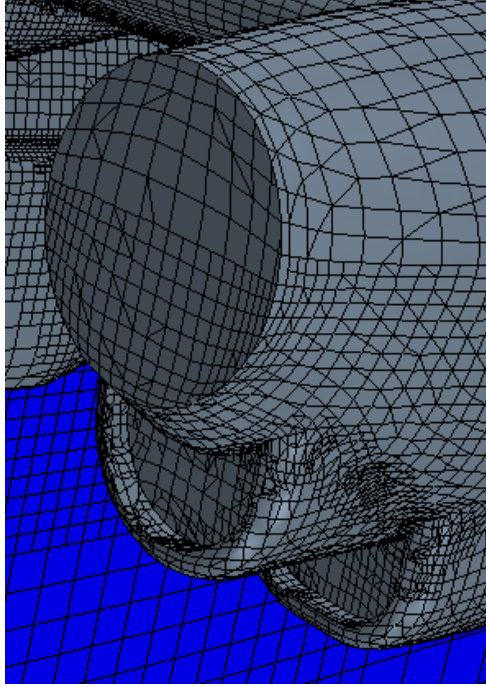
2.5 Mesh

The selection of mesh options is known to be critical for solution accuracy. The following mesh models were used for all simulations:

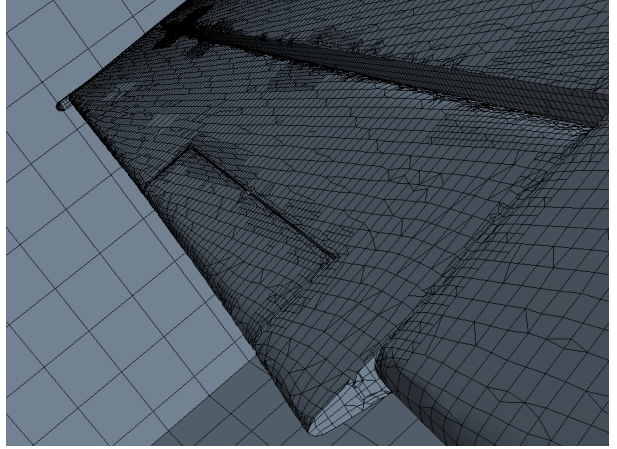
1. **Prism Layer Mesher:** The near wall prism layer thickness is the only means that the user can influence the y_w^+ value, which is critical for simulation validity. As discussed in Section 2.4, y_w^+ depends on wall shear stress, fluid density and kinematic viscosity. To generate initial grids, the near wall prism layer thickness was estimated using a Schlichting skin-friction y^+ wall distance formula [4], taking characteristic length and

velocity scales as the plane length and cruise speed respectively. In the final grids, the total thickness of the prism layer was matched to the approximate average boundary layer thickness. This thickness was estimated from initial rough simulations. From the total boundary layer thickness and the first layer thickness, the number of prism layers was selected to achieve a stretching factor below 1.3.

2. **Surface Remesher:** All grids were checked to ensure that aircraft model was properly represented. Areas of particular concern were the wing flaps and engine ‘intakes’ because of the complexity of the geometry. Good representation of these regions was achieved by setting the surface size on the airplane body to appropriate values. The fidelity of the representation was evaluated through qualitative inspection. Figure 2.1a and 2.1b show the engine intake and wing flaps in the reference grid.
3. **Trimmer:** Used to generate a good quality volume mesh with computational efficiency [5].
4. **Volumetric Controls:** A volumetric control was employed to refine the grid around the plane and in the wake region. In this region, the flow field varies significantly. A finer grid allows better resolution of the variation in flow fields, e.g. velocity and turbulent kinetic fields, and hence enhances prediction of flow separation. Once the refined volume was defined and the cell size relative to base was set, the global template and surface growth rates, and base size, were varied until a grid of approximately 2 million cells was produced.



(a) Engine intake



(b) Wing flaps

Figure 2.1: Views of mesh

2.6 Turbulence Models

All the turbulence models used in this study are formulated with the objective of offering closure to the Reynolds Averaged Navier-Stokes (RANS) equations, shown below. One means of achieving this is through estimating the value of the eddy viscosity.

$$\frac{\partial \bar{u}_j}{\partial x_j} = 0 \quad (2.3)$$

$$\frac{\partial \bar{u}_i}{\partial t} + \bar{u}_i \frac{\partial \bar{u}_i}{\partial x_j} = -\frac{1}{\rho} \frac{\partial P}{\partial x_j} + \frac{\partial}{\partial x_j} \left(\nu \left(\frac{\partial \bar{u}_i}{\partial x_j} + \frac{\partial \bar{u}_j}{\partial x_i} \right) - \bar{u}'_i \bar{u}'_j \right) \quad (2.4)$$

The eddy viscosity (ν_t) is critical for estimating the value of the Reynold stress ($-\bar{u}'_i \bar{u}'_j$) as follows:

$$-\bar{u}'_i \bar{u}'_j = \nu_t \left(\frac{\partial \bar{u}_i}{\partial x_j} + \frac{\partial \bar{u}_j}{\partial x_i} \right) - \frac{2}{3} \delta_{ij} k \quad (2.5)$$

k is the turbulent kinetic energy defined as follows:

$$k = u'_i u'_i + u'_j u'_j + u'_k u'_k \quad (2.6)$$

The three turbulence models considered in this study are described herein.

2.6.1 Standard $k - \epsilon$ two-layer all y_w^+ treatment

This model uses turbulent kinetic energy, k , and its dissipation rate, ϵ , to estimate the value of the eddy viscosity as an input into the RANS equations. These values vary throughout the flow and are dependent on their own transport equations, the coefficients of which are empirically determined. In this model, the eddy viscosity is calculated at each node as below:

$$\nu_t = c_\mu \frac{k^2}{\epsilon} \quad (2.7)$$

The transport equations for k and ϵ are reproduced below (for the standard model) [6] (note velocity quantities below are time averaged):

$$\rho \frac{\partial k}{\partial t} + \rho u_j \frac{\partial k}{\partial x_j} = \frac{\partial}{\partial x_j} \left(\frac{\mu_t}{\sigma_k} \frac{\partial k}{\partial x_j} \right) + \mu_t \left(\frac{\partial u_i}{\partial x_j} + \frac{\partial u_j}{\partial x_i} \right) \frac{\partial u_i}{\partial x_j} - \rho \epsilon \quad (2.8)$$

$$\rho \frac{\partial \epsilon}{\partial t} + \rho u_j \frac{\partial \epsilon}{\partial x_j} = \frac{\partial}{\partial x_j} \left(\frac{\mu_t}{\sigma_\epsilon} \frac{\partial \epsilon}{\partial x_j} \right) + c_{\epsilon 1} \frac{\epsilon}{k} \mu_t \left(\frac{\partial u_i}{\partial x_j} + \frac{\partial u_j}{\partial x_i} \right) \frac{\partial u_i}{\partial x_j} - c_{\epsilon 2} \rho \frac{\epsilon^2}{k} \quad (2.9)$$

The wall treatment is 'All y_w^+ ', and so either a wall-function or wall-resolved simulation will be selected automatically on the basis of y_w^+ as described in Section 2.4.

2.6.2 SST $k - \omega$

The SST $k - \omega$ model uses the $k - \epsilon$ model as above for free shear flows, and uses a different model, the $k - \omega$ model for near-wall flow. This is because of the tendency for the $k - \omega$ model to become inaccurate under high shear strains. The $k - \omega$ model uses the values of turbulent kinetic energy (k) and dissipation per unit kinetic energy (ω) to estimate the eddy viscosity (ν_t). The central estimate is shown below:

$$\nu_t = \frac{k}{\omega} \quad (2.10)$$

Where the specific dissipation is defined as follows:

$$\omega = \frac{\epsilon}{k c_\mu} \quad (2.11)$$

The transport equations for k and ω for this model are given below [7]:

$$\rho \frac{\partial k}{\partial t} + \rho u_j \frac{\partial k}{\partial u_j} = \frac{\partial}{\partial x_j} \left(\left(\mu + \frac{\mu_t}{\sigma_k^\omega} \right) \frac{\partial k}{\partial x_j} \right) + \mu_t \left(\frac{\partial u_i}{\partial x_j} + \frac{\partial u_j}{\partial x_i} \right) \frac{\partial u_i}{\partial x_j} - \rho \beta^* k \omega \quad (2.12)$$

$$\rho \frac{\partial \omega}{\partial t} + \rho u_j \frac{\partial \omega}{\partial u_j} = \frac{\partial}{\partial x_j} \left(\left(\mu + \frac{\mu_t}{\sigma_\omega} \right) \frac{\partial \omega}{\partial x_j} \right) + \alpha \frac{\omega}{k} \left(\frac{\partial u_i}{\partial x_j} + \frac{\partial u_j}{\partial x_i} \right) \frac{\partial u_i}{\partial x_j} - \rho \beta \omega^2 \quad (2.13)$$

This estimation for the eddy viscosity is known for accurately predicting flow separation [7], which is critical when predicting stall angles of an aircraft.

2.6.3 Quadratic pressure strain Reynolds stress with high y_w^+ treatment

The Reynold Stress Model, unlike the $k - \epsilon$ and $SSTk - \omega$ models, does not manifest via the conduit of eddy viscosity. It is a second-moment closure model that relies on directly solving for the Reynolds stress tensor ($\overline{u'_i u'_j}$) [8]. The full transport equation modelling the Reynolds stress tensor is given below [9]:

$$\begin{aligned} \rho \frac{\partial \overline{u'_i u'_j}}{\partial t} + \rho \overline{u_k} \frac{\partial \overline{u'_i u'_j}}{\partial x_k} &= \rho \left(\overline{u'_i u'_k} \frac{\overline{u_j}}{\partial x_k} + \overline{u'_j u'_k} \frac{\partial \overline{u_i}}{\partial x_k} \right) - \overline{p' \left(\frac{\partial u'_i}{\partial x_j} + \frac{\partial u'_j}{\partial x_i} \right)} \\ &\quad - 2\mu \overline{\frac{\partial u'_i}{\partial x_k} \frac{\partial u'_j}{\partial x_k}} + \frac{\partial}{\partial x_k} (\overline{p' u'_i} \delta_{jk} + \overline{p' u'_j} \delta_{ik} + \overline{p' u'_k} \delta_{ij}) \end{aligned} \quad (2.14)$$

This model is generally referred to by the abbreviation 'QPS' for the remainder of this report.

3. Results and Discussion

3.1 Grid Refinement Study

A study was conducted to evaluate grid-dependence of key flow parameters (in the context of this project, these are the lift and drag coefficients). Grids of increasing number of cells were produced and simulations were ran for the most computationally demanding flow case – cruise – for all three turbulence models.

The grid sizes and study outputs are given in Tables 3.1, 3.2 and 3.3 for the $k - \epsilon$, $k - \omega$ and QPS models respectively. The drag coefficient and lift coefficient are plotted against number of cells in Figure 3.1a and 3.1b respectively.

A limit of approximately 2 million cells was set for the reference grid. It was decided to use approximately 200,000 cells for the coarse grid and 4 million cells for the fine grid to cover a wide range of grid sizes within the limits of the available computational resources. The grids were generated based on changes to the base cell size. To ensure reasonable y_w^+ values and hence valid grids in all cases, the thickness of the near wall prism layer was kept the same for all grids.

Table 3.1: Grid refinement study for $k - \epsilon$ model;

Turbulence Model		$k - \epsilon$		
No. Cells	Avg. Y^+	C_D	C_L	L/D
216530	174.104	0.069	0.551	7.965
2084163	69.893	0.046	0.507	11.115
3919650	67.926	0.042	0.487	11.469

Table 3.2: Grid refinement study for $k - \omega$ model;

Turbulence Model		$k - \omega$		
No. Cells	Avg. Y^+	C_D	C_L	L/D
216530	144.628	0.069	0.551	7.939
2084163	65.203	0.045	0.498	11.026
3919650	61.318	0.041	0.466	11.390

Table 3.3: Grid refinement study for *QPS* model;

Turbulence Model	<i>QPS</i>			
No. Cells	Avg. Y^+	C_D	C_L	L/D
216530	143.550	0.069	0.542	7.848
2084163	68.499	0.045	0.499	11.008
3919650	64.782	0.041	0.472	11.440

For all turbulence models, Figure 3.1a shows significant change in drag coefficient between the coarse and reference grids (-34.4% for *QPS*) and much smaller change in drag coefficient between the reference and fine grids (-9.0% for *QPS*). Though of course a finer grid offers better results, the improvements in convergence diminish significantly above the reference grid and the reference grid is deemed suitably converged for drag coefficient. The coarse mesh does not allow for full resolution of interesting flow features. For example, in the wake region the velocity field varies significantly and in this region phenomena such as flow separation and vortex shedding occur. These phenomena have a significant influence on drag and drag coefficient and offer some explanation of the poor coarse grid performance.

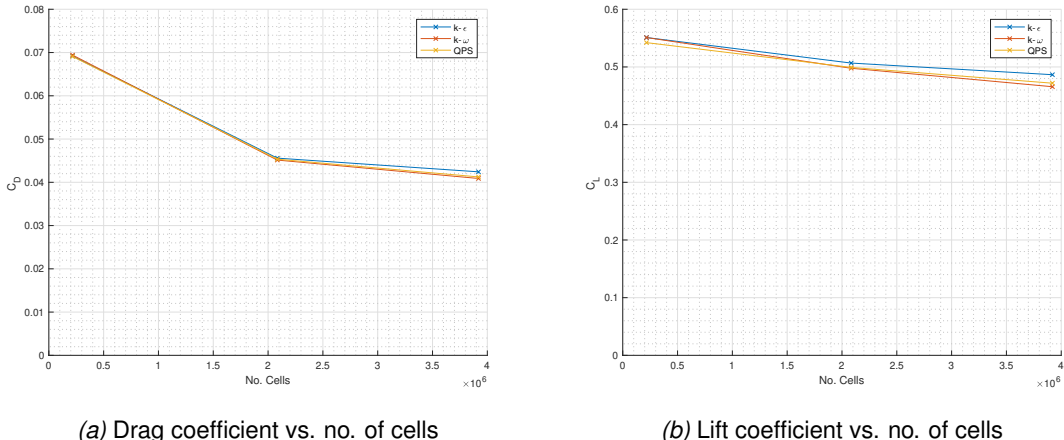


Figure 3.1: Grid refinement study results

The smaller changes in lift coefficient with grid size are much smaller than those found for drag coefficient, as shown in Figure 3.1b. It is therefore concluded that reasonable grid independence for the integral quantities concerned – lift and drag coefficients – is achieved with the reference mesh.

All of turbulence models vary similarly with grid size. Though only three grids were considered, this gives reason to believe that the solutions converge to grid independence at a similar rate. For each turbulence model, though the numerical solution does not match its true grid-independent solution, the differences between solutions and grid-independent solutions are similar. This means that comparisons between different turbulence model solutions, even

when not fully grid-independent, can illuminate meaningful physics-based differences between the turbulence models.

3.2 Analysis of Flight Physics

3.2.1 Qualitative Turbulence Model Comparison

The three turbulence models were compared qualitatively as the angle of attack of the plane was varied between -5° and 15° in 5° increments.

Angle of Attack vs Wing Pressure

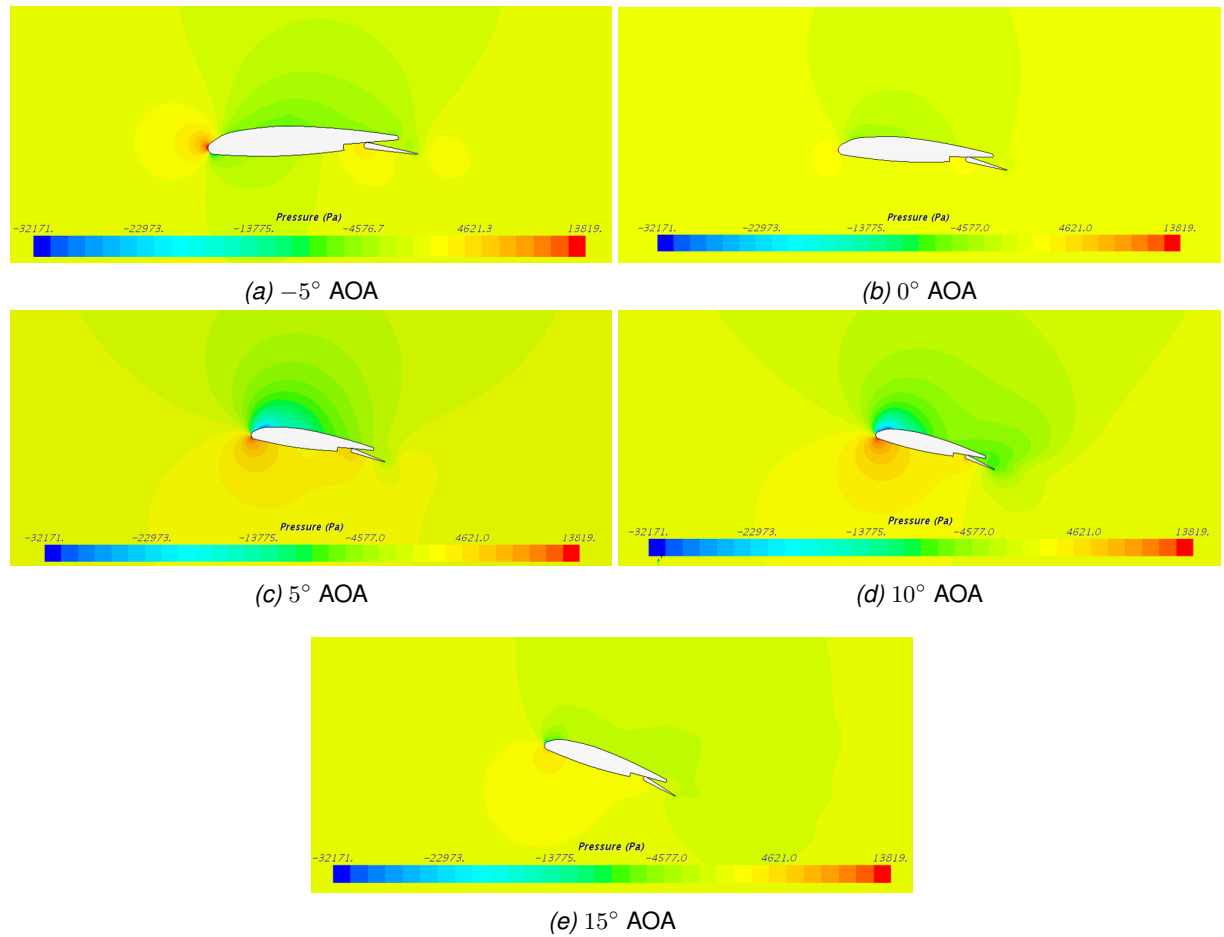


Figure 3.2: Pressure field at different angles of attack using $k - \omega$ model

The impact of angle of attack (AOA) on pressure over the wing was investigated. The $k - \omega$ model was chosen for comparison of pressure over $k - \epsilon$, as the $k - \epsilon$ model is poor at dealing with adverse pressure gradients which are expected to become stronger as angle of attack is increased [10]. It is evident from Figure 3.2 that increasing the AOA increases the

pressure differential over the wing until separation occurs, which is shown in Figure 3.2e. It can be interpreted from this result that lift increases with AOA until the onset of separation, as expected.

10° Angle of Attack Study

Figure 3.3 displays the velocity field approximately 8 metres from the wing tip using the three turbulence models at an angle of attack of 10 degrees. There is no separation visible along the top surface of the wing. The flow around the wing is as expected – the flow has a high velocity region above the wing and low velocity region below the plane. Vortices above the wing flap are visible for all three turbulence models.

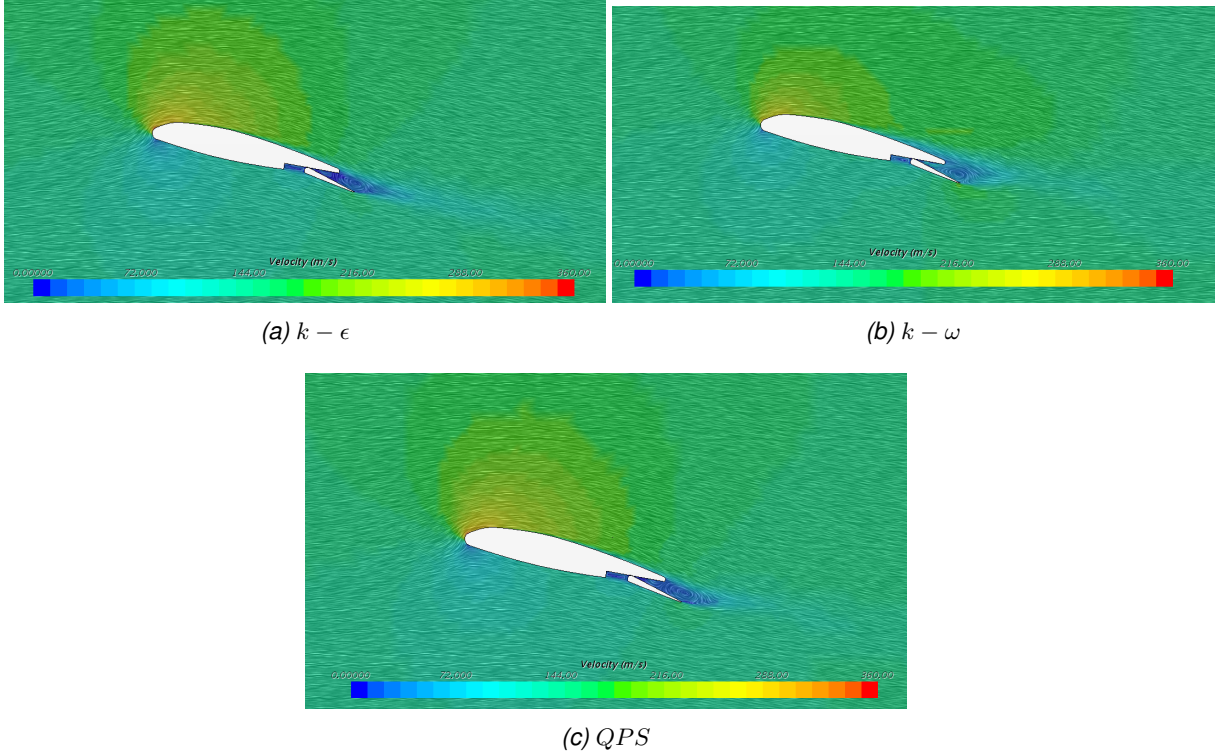


Figure 3.3: Velocity field at 10° AOA, 8m from wing tip

The velocity field was also investigated closer to the wing tip. Figure 3.3 shows the velocity field for the three turbulence models approximately 2 metres from the wing tip. Both the $k - \epsilon$ and QPS models display flow around the wing with no separation, however, the $k - \omega$ model shows significant separation. This is consistent with literature which suggests that the $k - \omega$ model predicts separation earlier than other models, as one of the shortcomings of the $k - \epsilon$ model is the inability to cope with adverse pressure gradients [10], thus cannot accurately predict separation. The separation for the $k - \omega$ model begins at the upper leading edge of the wing, and large eddies in the flow are visible inside the separation region.

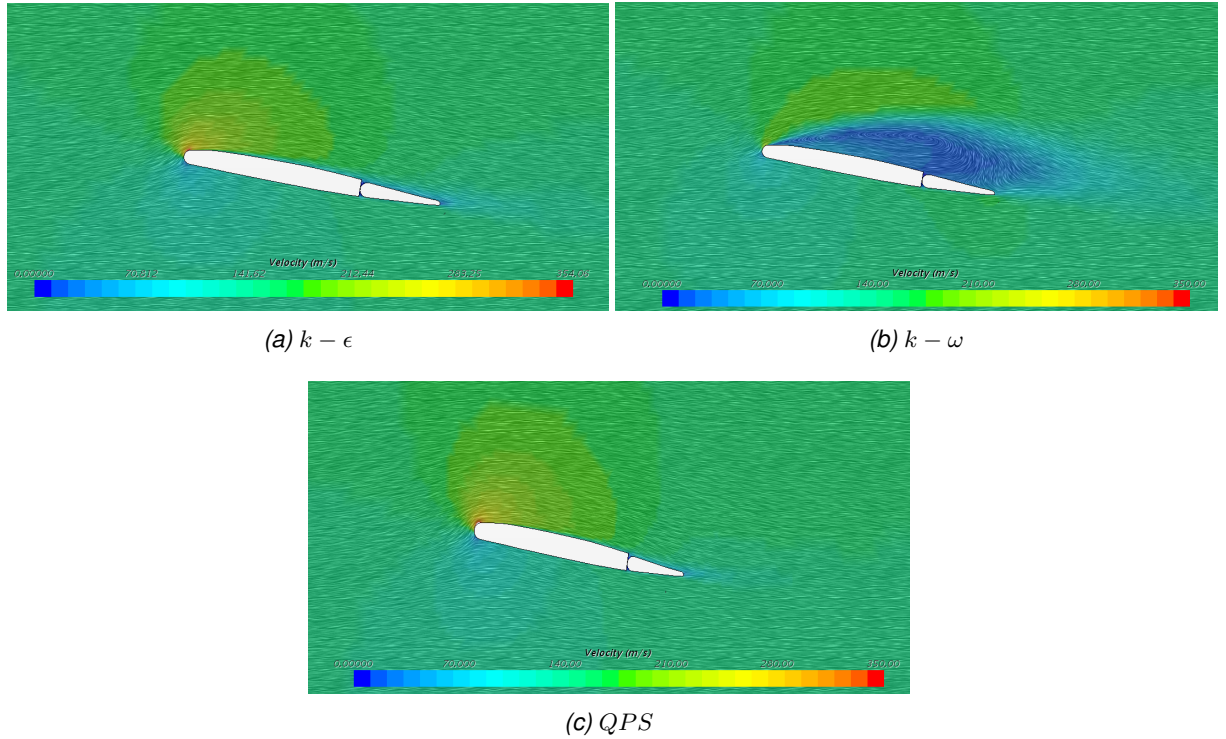


Figure 3.4: Velocity field at 10° AOA, 2m from wing tip

Variations of pressure and turbulent kinetic energy (TKE = k) were also investigated at this location and are shown in Figures 3.5 and 3.6 respectively. The region of high TKE for the $k - \omega$ model is due to the detachment of the flow from the wing, resulting in high velocity fluctuations in that region, which are indicated in Figure 3.4. The TKE around the wing for the $k - \epsilon$ and QPS models are much lower, as no separation is predicted. Figure 3.5 displays the low pressure region along the top surface of the wing for the $k - \omega$ model which is characteristic of flow separation. Both of the other models are displaying a pressure map typical of flow over an airfoil, with a high pressure region on the bottom and low pressure region over the top surface.

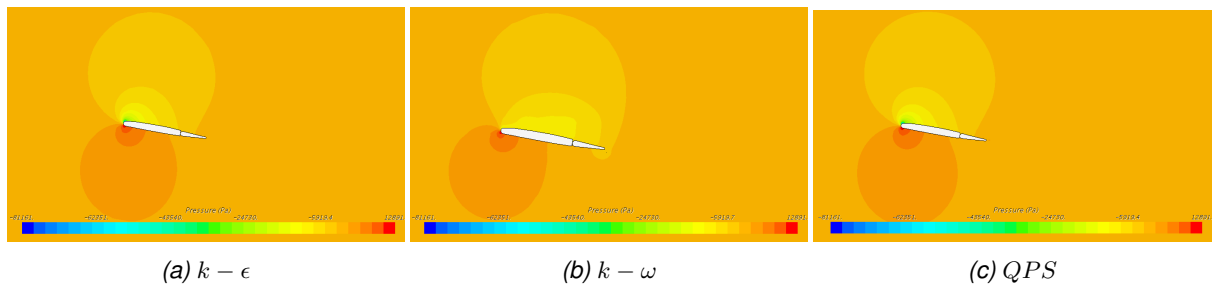


Figure 3.5: Pressure field at 10° AOA, 2m from wing tip

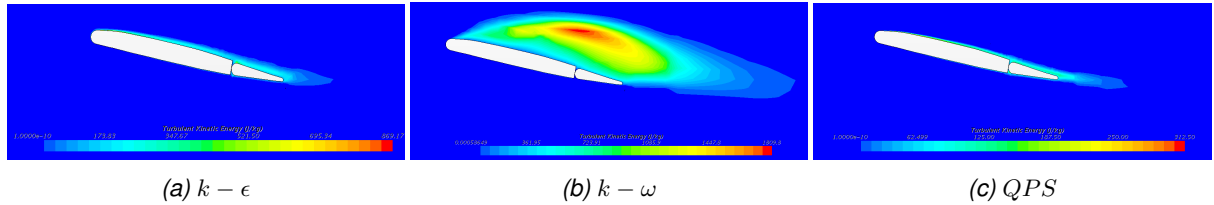


Figure 3.6: Turbulent Kinetic Energy at 10° AOA, 2m from wing tip

15° Angle of Attack Study

At an angle of attack of 15°, flow separation has occurred for all three models at 2 m and 8 m from the wing tip, which is shown by the velocity fields shown in Figure 3.7. As the angle of attack is increased, the adverse pressure gradient also increases, eventually causing flow separation, as the flow cannot remain attached to the surface of the wing.

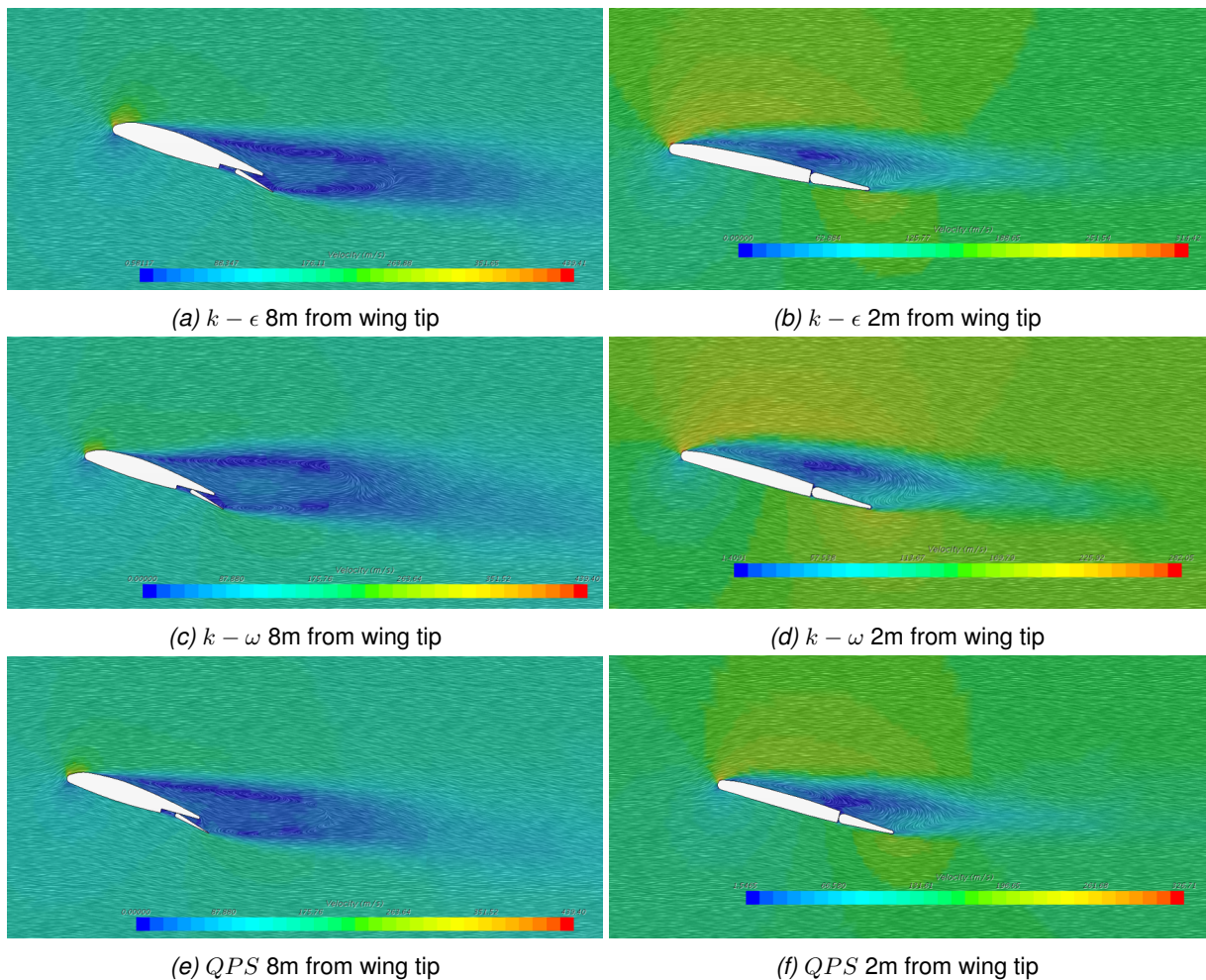


Figure 3.7: Velocity field at 15° AOA

The intensity of turbulence in the recirculation region for each turbulence model was quantified by plotting the TKE over the wing, which is shown in Figure 3.8. The recirculation region for the $k - \omega$ model is the largest, as it predicts flow separation before other models. All

three turbulence models are showing two regions with high TKE, one from flow detachment on the top side of the wing and from vortices shed at the edge of the wing flap. In theory, the *QPS* model should give the most accurate result, as it is a Reynolds stress model which can account for anisotropy in the flow. An underlying assumption of eddy viscosity models such as the $k - \omega$ and $k - \epsilon$ models is that the turbulence is isotropic, therefore it should give a less accurate representation of the flow in the wake which is anisotropic [10].

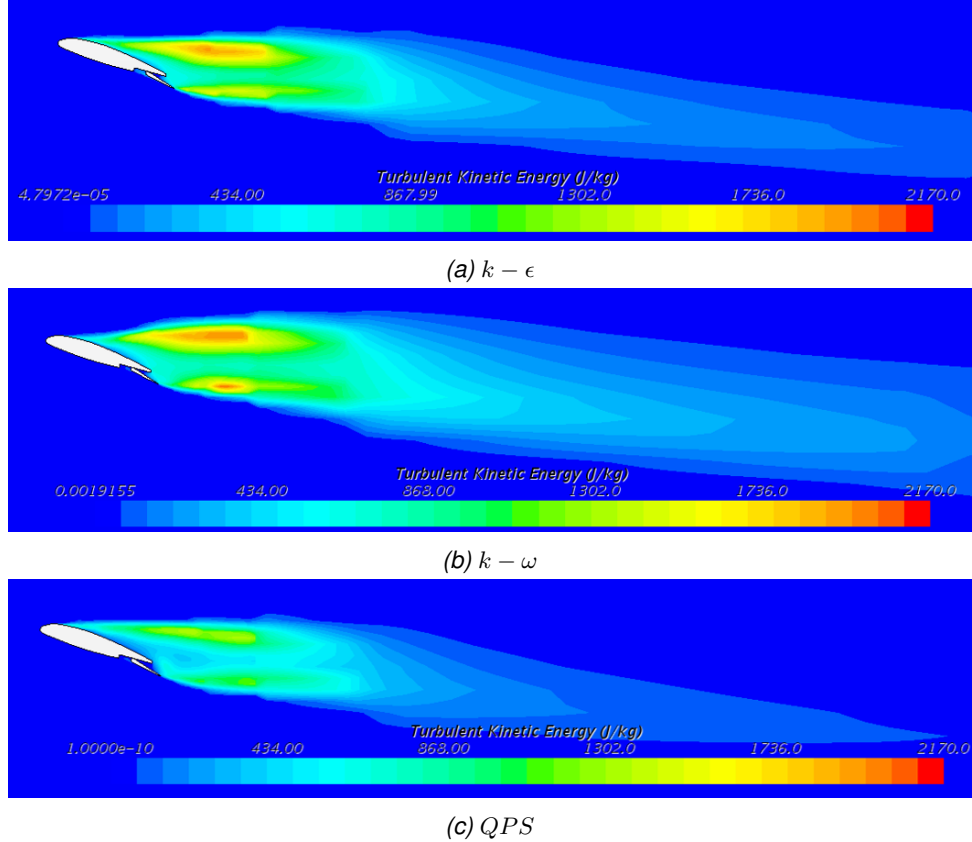


Figure 3.8: Turbulent Kinetic Energy at 15° AOA, 8m from wing tip

3.2.2 Lift and Drag Turbulence Model Comparison

The results of the study investigating the effect of angle of attack and turbulence model on the lift and drag coefficients of the aircraft are shown in Table 3.4 and Figure 3.9.

The results show that the three turbulence models are broadly in agreement with respect to the values calculated for C_L , C_D and L/D across all angles apart from 10°. This is due to the $k - \omega$ model predicting flow separation at and above this angle of attack, whereas other models only begin to separate at larger angles of attack. This can be seen in the Figures presented in Section 3.2.1. The SST $k - \omega$ model is known for accurately predicting flow separation [7] such that the results for this turbulence model are more likely to be correct at

Table 3.4: C_D , C_L & L/D for different turbulence models and angles of attack;

Turbulence Model	$k - \epsilon$			$k - \omega$			QPS		
Angle of Attack	C_D	C_L	L/D	C_D	C_L	L/D	C_D	C_L	L/D
-5	0.099	0.204	2.059	0.098	0.266	2.709	0.099	0.232	2.340
0	0.046	0.507	11.110	0.045	0.499	11.040	0.045	0.499	11.008
5	0.182	2.586	14.245	0.182	2.574	14.126	0.182	2.577	14.144
10	0.289	3.586	12.391	0.358	2.746	7.675	0.277	3.488	12.591
15	0.210	0.879	4.189	0.210	0.769	3.672	0.201	0.760	3.785

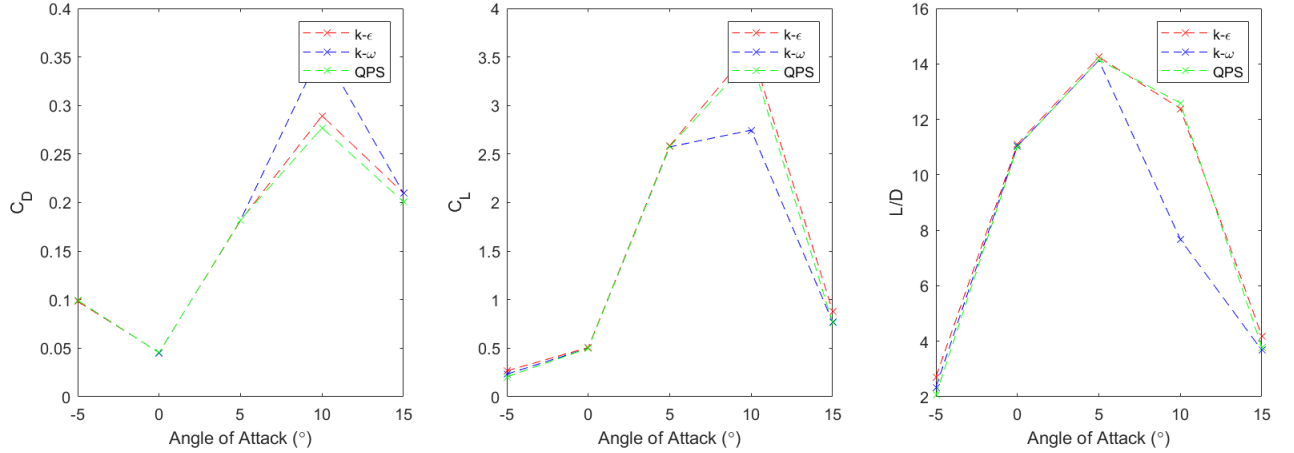


Figure 3.9: Graph of C_D , C_L & L/D for different turbulence models and angles of attack,;

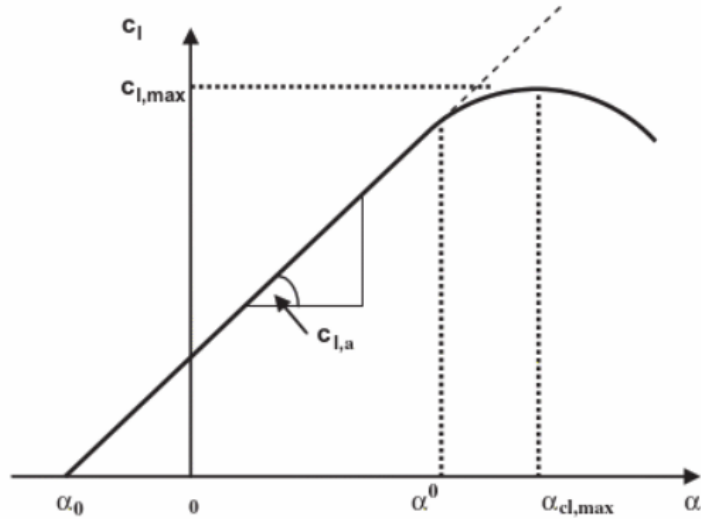


Figure 3.10: C_L vs angle of attack [11]

10° angle of attack.

From Figure 3.9 it is seen that flow is separated in the $k - \omega$ model but not the $k - \epsilon$ or QPS. The flow separation results in higher drag and lower lift, as shown in Figure 3.9. The general trend of the lift coefficient is consistent with the literature, which is illustrated in Figure 3.10. The lift coefficient shows agreement with literature, which claims a C130 has a constant

lift coefficient of 1.95 during takeoff [12]. NASA [12] also assumes a drag coefficient of 0.209 for takeoff, which is higher than simulation results at the $C_L = 1.95$. This could be due to neglecting the effect of the propellers in simulation, which could introduce increased levels of turbulence and therefore drag over the wing. This agrees with results; Figure 3.2 shows separation (and therefore increased turbulence) increases drag for a given lift. The maximum Lift/Drag ratio for a C130 plane is quoted as approximately 17 [12]. This is in good agreement with the simulation results where a maximum of 14.245 was found for the $k - \epsilon$ model at 10 degrees. The maximum value calculated by the simulation would also likely be higher, as the data collected only suggests a maximum L/D between 0 and 10 degrees. It is not fair to assume the maximum is at 5 degrees angle of attack. It is worth noting that NASA [12] considers a C130 at sea-level rather than at cruise altitude where compressibility effects are more impactful.

3.2.3 Take-off Speed Turbulence Model Comparison

The take-off speed is the velocity of the plane at which the lift to weight (L/W) is equal to 1. The weight was taken as $337120N$ [1] and the lift was calculated using the following equation:

$$Lift = \frac{1}{2}C_L\rho Au^2 \quad (3.1)$$

The wing area was taken as $162m^2$ [1]. The density was taken as the air density at Albuquerque airport, New Mexico, United States which is $1.041kg/m^3$ [13] as this is one of the hardest airports to take off from in the world due to its low air density. This is due to a combination of its hot climate and high altitude. The aircraft was assumed to be taking off at an angle of attack of 5 degrees.

Star-CCM+ CFD simulations were run at a range of velocities ($40, 50, 60, 70, 80, 90ms^{-1}$) using three different turbulence models, namely $k - \epsilon$, $k - \omega$ and QPS . A quadratic fit was then used to determine the take-off speeds more accurately. The results are shown in Figure 3.11 and the predicted take off speeds are shown by the circles. These predicted take off speeds were verified with further simulations and the results are listed in Table 3.5 below. The take-off speeds from the three models are in agreement to two significant figures (variation in the results is $0.5 ms^{-1}$). The $k - \epsilon$ model predicts the lowest take-off speed ($61.5ms^{-1}$) and the $k - \omega$ model the highest ($62.0ms^{-1}$).

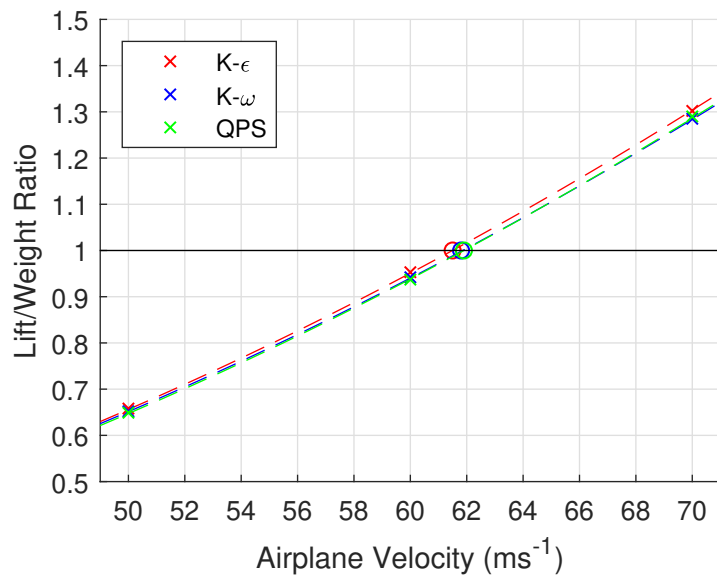


Figure 3.11: Graph showing take-off speed for different turbulence models;

Table 3.5: Predicted take-off speed for different turbulence models;

Turbulence model	Take-off Speed	L/W
$k - \epsilon$	61.5	1.0022
$k - \omega$	62.0	1.0032
QPS	61.8	1.0047

4. Future Work

Much of the work in this report is best considered a precursor to a fuller, more detailed CFD study of the C130 airframe. Good modelling practices have been followed throughout the current study but various constraints have meant that the produced results are at best preliminary.

For example, exceeding the two million cell limit for the reference mesh would have provided better founded and more accurate results. Although solutions were deemed sufficiently grid independent (Section 3.1), variation in the drag and lift coefficients between the reference mesh and fine mesh was observed. Re-running simulations (for both the take-off speed and angle of attack studies) with a finer mesh would yield results that are closer to 'true' solutions. This would allow for better comparisons between the turbulence models and enable predictions of lift and drag coefficients that are true to the turbulence models.

For optimal study validity, grid-independence should be evaluated for all of the cases considered (certainly for the high angle of attack simulations, where the flow is complex and computationally demanding). Due to time constraints, only 0° AOA cruise was evaluated for grid independence.

The angle of attack simulations indicate that a maximum lift-to-drag ratio occurs at some angle of attack between 0° and 10° . Due to the coarseness of the results - angles of attack were evaluated in 5° increments - no more precise value can be given. Conducting simulations at more points within this range would allow for this maximum to be pinpointed with greater accuracy. Conducting more angle of attack simulations would also allow for a more precise analysis of flow separation, i.e. the specific angle of attack at which flow separation occurs and regions on the wing where separation first occurs etc.

There is much room for further exploration of take-off. One drawback of the current study was that ground effects were neglected - the ground was modelled as a slip wall in an effort to reduce the computational expense of an additional prism layer. This assumption is not true and the ground should be modelled with a no-slip boundary condition.

The take-off speed was only computed for one angle of attack (5°). The take-off speed of

course varies with angle attack and its variation with angle of attack would be interesting to investigate. During take-off, wing geometry is often altered to give desired aerodynamic performance (for example, the deployment of flaps). This could be investigated. So too the effect of closeness to the ground could be investigated.

Simplifications were made to the aircraft geometry that may significantly impact aerodynamic performance. As discussed in Section 3.2.2, the engine propellers were not modelled and may significantly impact flow over the wings. During take-off, the landing gear was not modelled which again significantly impacts aerodynamics.

A comparison of the study results to results found through some other means would give the study greater credibility, and would indicate whether or not the found results are credible. Data from experiments or from future Large Eddy Simulation studies could be used.

5. Conclusions

This report investigated the aerodynamics of the Hercules C130 for three different turbulence models: standard $k - \epsilon$ two-layer all y_w^+ treatment, SST $k - \omega$ and quadratic pressure strain Reynolds stress with high y_w^+ treatment.

The report found that with 2 million cells, the simulation is close to grid independence as indicated by the diminishing change in lift and drag coefficients with increasing cell numbers. This was the case for all turbulence models considered.

Take-off speed was found to be $61.5 - 62 ms^{-1}$ for the three turbulence models when an angle of attack of 5° is employed. This was also the largest angle of attack considered that did not exhibit full separation for at least one of the turbulence models.

As expected, the simulated L/D curve exhibited a maximum around 5° . All turbulence models were in broad agreement for all angles of attack investigated except for 10° . At this angle, the $k - \omega$ model predicted full separation when the others did not. This led to higher drag and lower lift coefficients. The predicted drag and lift coefficients are broadly in alignment with those found in the literature.

6. References

- [1] RAF. Hercules C130J Specifications, 2020. URL
<https://www.raf.mod.uk/aircraft/c-130j-hercules/>.
- [2] P. Aleiferis. An Introduction to the Commercial CFD Code STAR-CCM+. Instructional Document, 2019.
- [3] B.E. Launder and D.B. Spalding. The numerical computation of turbulent flows. *Computer Methods in Applied Mechanics and Engineering*, 3:269–289, 1974.
- [4] Hermann Schlichting and Klaus Gersten. *Boundary-layer theory*. Springer, 2016.
- [5] CD-ADAPCO. STAR-CCM+ Documentation, 2020.
- [6] W.P. Jones and B.E. Launder. The prediction of laminarization with a two-equation model of turbulence. *International Journal of Heat and Mass Transfer*, 15:301–314, 1972.
- [7] D.C. Wilcox. Re-assessment of the scale-determining equation for advanced turbulence models. *AIAA Journal*, 26:1299–1310, 1988.
- [8] B.E. Launder, G.J. Reece, and W. Rodi. Progress in the development of a reynolds stress turbulence closure. *Journal of Fluid Mechanics*, 68:537 – 566, 1975.
- [9] P. Aleiferis. Computational Fluid Dynamics (CFD) (MECH97012/MECH97052, ME4 & MSc), 2019. Lecture Slides.
- [10] Ideen Sadrehaghghi. Turbulence modeling - a review. Technical report, 03 2020.
- [11] P. M. Sforza. *Commercial Airplane Design Principles*. Elsevier Aerospace Engineering, 2014.
- [12] A.P. Kottapalli and F.D. Harris. Converting a c-130 hercules into a compound helicopter: A conceptual design study. URL
<https://ntrs.nasa.gov/archive/nasa/casi.ntrs.nasa.gov/20100023291.pdf>.
- [13] Air Density Online. Albuquerque Airport Air Density, 2020. URL
https://airdensityonline.com/track-results/Albuquerque_Dragway/.